Version: Accepted Version

GPRInvNet: Deep Learning-Based Ground Penetrating Radar Data Inversion for Tunnel Lining

Bin Liu, Yuxiao Ren, Hanchi Liu, Hui Xu, Zhengfang Wang,
Anthony G. Cohn, and Peng Jiang, *Member, IEEE*

Abstract—A DNN architecture called GPRInvNet is proposed to tackle the challenge of mapping Ground Penetrating Radar (GPR) B-Scan data to complex permittivity maps of subsurface structure. GPRInvNet consists of a trace-to-trace encoder and a decoder. It is specially designed to take account of the characteristics of GPR inversion when faced with complex GPR B-Scan data as well as addressing the spatial alignment issue between time-series B-Scan data and spatial permittivity maps. It fuses features from several adjacent traces on the B-Scan data to enhance each trace, and then further condense the features of each trace separately. The sensitive zone on the permittivity map spatially aligned to the enhanced trace is reconstructed accurately. GPRInvNet has been utilized to reconstruct the permittivity map of tunnel linings. A diverse range of dielectric models of tunnel lining containing complex defects has been reconstructed using GPRInvNet, and results demonstrate that GPRInvNet is capable of effectively reconstructing complex tunnel lining defects with clear boundaries. Comparative results with existing baseline methods also demonstrate the superiority of the GPRInvNet. To generalize GPRInvNet to real GPR data, we integrated background noise patches recorded form a practical model testing into synthetic GPR data to train GPRInvNet. The model testing has been conducted for validation, and experimental results show that GPRInvNet achieves satisfactory results on real data.

Index Terms—Ground-penetrating radar, GPR data inversion, Tunnel lining detection, Deep neural networks

I. INTRODUCTION

GROUND penetrating radar (GPR) has been extensively used in many applications, such as glaciology, archaeology, and civil and geotechnical engineering. For example, it has been used for geological surveys, buried object detection, and detection of subsurface structures [1]-[3]. Among these applications, the non-destructive inspection of tunnel lining structure is popular [4]-[5]. GPR transmits an electromagnetic wave into the tunnel lining structure and receives echoes to form B-scan images, from which the structural condition of the tunnel lining can be deduced [6]-[7]. The inspection of the structural condition of tunnel lining is of great importance to the safe operation of tunnels [8]. However, due to geological and environmental factors, ageing, increased loading, man-made impacts, and irregular construction, tunnel linings progressively deteriorate, which leads to many defects, such as lining voids, cracks, delamination, lining leakage, and non-compactness of concrete. These covert defects, which are generally inside the tunnel lining, may reduce the bearing capacity of the lining, affect normal operation, shorten tunnel durability, or even induce incidents [9]-[10]. Several incidents have occurred due to the deterioration of tunnel lining structures, such as the Big Dig ceiling collapse in 2006 in Boston and the Sasago Tunnel collapse in 2012 in Tokyo [11].

The translation of the electromagnetic information stored in the B-Scan into inner-defect related information, such as locations, shapes, and dielectric properties, is of great importance for tunnel lining defect inspection. There are a number of existing methods for GPR inversion which aim to map the dielectric distribution of the structure to be detected based on the recorded GPR data [12]. These methods mainly include common-midpoint velocity analysis [13], ray-based methods [14], reverse-time migration (RTM) [15], tomography approaches [16], and full-waveform inversion (FWI) methods [17]-[18]. Among these methods, FWI is the state-of-art solution to qualitatively and quantitatively reconstruct images of structures. It directly employs the entire received waveforms to match with the forward modeled data; it then reconstructs the dielectric distributions of the structures by minimizing the misfit between these two sets of data [19]-[20]. FWI originated

B. Liu, Y. Ren and H. Xu are also with the Geotechnical @ Structural Engineering Techniques Research Center, Shandong University, Jinan, 250061, China. (email: liubin0635@163.com; ryxchina@gmail.com and 1162259518@qq.com).

H. Liu and Z. Wang are with the School of Control Science and Engineering, Shandong University, Jinan, 250061, China. (email: 201934495@mail.sdu.edu.cn; wangzhengfangsdu@hotmail.com).

A. Cohn is with the School of Computing, University of Leeds, Leeds, LS2 9JT, UK (e-mail: A.G.Cohn@leeds.ac.uk), and is an Adjunct Professor at Shandong University.

in the field of seismic exploration [21] and has been rapidly employed for processing radar data since [22]. In tunnel lining-related applications, some developments of FWI have been presented to further improve performance, including a truncated Newton method based on GPR FWI with structural constraints [23], a multi-scale inversion strategy and bi-parametric FWI method [24], and a combination of improved FWI and RTM [25]. However, because tunnel lining defects always have irregular geometries and complex distributions, the received subsurface GPR data are generally interlaced and accompanied by discontinuous and distorted echoes. Furthermore, some strong echoes induced by the steel rebar in tunnel linings may mask the signature of defects. In such cases, the B-scan images commonly show "pseudo-hyperbolic" morphologies or clutter [24]. Thus, it is challenging for traditional FWI to precisely reconstruct the dielectric distribution of the target. The location of defects may be wrongly computed, notwithstanding the considerable computational cost of FWI methods.

In recent years, deep neural networks (DNNs) have demonstrated extraordinary abilities in applications related to image classification [26]-[27], object detection [28], semantic segmentation (pixel-level prediction)[29]-[30], and image synthesis [31]. DNNs automatically learn high-level features from training data and then estimate a nonlinear mapping between input image data and various data domains, such as labels, text, or other images. Accordingly, some end-to-end deep learning-based inversion methods have been introduced to invert the velocity or impedance from seismic data. Das et al. utilized a 1D convolutional neural network (CNN) to predict high-resolution impedance [32]. Araya-Polo et al. proposed GeoDNN for seismic tomography [33]. Alfarraj et al. proposed a semi-supervised framework for impedance inversion based on convolutional and recurrent neural networks [34]. For velocity inversion, Zhang et al. developed an end-to-end framework called VelocityGAN to reconstruct subsurface velocity directly from raw seismic waveform data [35]. Wu et al. designed InversionNet, which follows the auto-encoder architecture to map seismic data to a corresponding velocity model [36]. In our previous study, we proposed the DNN-based SeisInvNet model to address weak spatial correspondence, the uncertain reflection-reception relationship between seismic data and velocity model, and the time-varying problem of seismic data [37]. SeisInvNet can recover the details of interfaces and accurately reconstruct the velocity model.

Because GPR and seismology are both wave-based geophysical techniques, these state-of-the-art methods for seismic inversion bring new perspectives for addressing the GPR inversion problem. However, it may not be an optimal choice to directly utilize existing DNNs designed for seismic inversion to process GPR data. First, because defects usually have irregular geometry and inhomogeneous distributions, the rebar or complex dielectric distributions in the tunnel lining may mask the effective GPR signals reflected by the defects. In such cases, the GPR data of the tunnel lining is usually more complex than the seismic data. Therefore, the DNNs for GPR data inversion should have strong abilities to extract effective features from complex data. Secondly, GPR data has unique spatial alignment characteristics: unlike the seismic case, the relation between the reflection and reception [37] of GPR is relatively certain as it has one transmitter and one receiver. Additionally, as the electromagnetic waves of GPR show a faster decay than seismic waves, most of the useful signals induced by one defect are captured in several adjacent GPR traces rather than the traces far from the defect. Therefore, to accurately reconstruct the local details of the permittivity map using DNNs, it is better to make full use of the information extracted from adjacent GPR traces rather than the global context, which avoids learning from ineffective information.

So far, little progress has been made in DNN-based GPR data inversion. Most existing studies have adopted DNNs to process GPR B-Scan data for the detection of buried object [38] and rebars [39], identification of subgrade defects [40], or reconstruction of concealed crack profiles in pavements [41]. These methods were focused on the tasks of classification or object detection in GPR B-Scan images, where the output is class labels or locations of defects in the B-scan images rather than the subsurface images of the structures. In terms of mapping a GPR B-Scan image to a subsurface image, to the best of our knowledge, the only study published so far was by Alvarez et al., who adopted some deep learning networks for GPR image-to-image translation [42]. Three widespread DNNs, Enc-Dec, U-Net, and generative adversarial network (GAN), were employed to reconstruct subsurface images of concrete sewer pipes from GPR B-Scan images. The methods were validated using synthetic data, and the results indicated the feasibility of utilizing DNNs to map a GPR image to a subsurface image of a structure. This study successfully reconstructed subsurface images containing defects with regular geometries (triangles, circles, and rectangles). However, the dielectric properties of the structure were not reconstructed.

To accurately invert dielectric properties of the tunnel lining and reconstruct complex defects with irregular geometries, an end-to-end DNN framework is proposed in this study. The proposed framework is called GPRInvNet, which consists of a specially designed "trace-to-trace" encoding process and a decoding process. The encoder enhances the features of each GPR trace using the information extracted from its adjacent traces. Then, we condense the features of each trace one-by-one to generate a group of features that spatially correspond to its own sensitive zone on the permittivity map. By doing so, we can extract effective features from complex B-Scan data and retain the spatial alignment between the input and output. GPRInvNet was first validated on a synthetic GPR dataset. A diverse range of dielectric models containing complex defects has been reconstructed using GPRInvNet, and a comprehensive comparative analysis has been performed. Furthermore, to apply our model to real GPR data, we integrated background noise patches recorded form the real world into synthetic GPR data to train our GPRInvNet. The experimental results demonstrate that our method provides good results on real GPR data.

The main contributions of this study are as follows:

1) We propose GPRInvNet to accurately invert dielectric

images directly from GPR data. To the best of our knowledge, this is the first deep learning-based network specifically designed for GPR data inversion.

2) We successfully apply GPRInvNet to reconstruct permittivity maps of tunnel linings containing complex defects. Comparative validation results demonstrate the superior performance of the proposed model against other baseline models.

3) We present a method to generalize GPRInvNet to real data. The experimental results for model testing show that method achieves satisfactory results on real data.

II. RELATED WORKS

A. Seismic Inversion

DNNs have been extensively exploited in seismology. Because GPR and seismology are both wave-based geophysical techniques, they share similar properties from a data processing perspective. Therefore, in this section, we introduce related works in the area of seismic inversion. Different approaches based on deep learning have been proposed recently for seismic inversion. Seismic inversion has been attempted using CNNs [32], recurrent neural networks [34] and GANs[35]. Furthermore, some DNN improvements have also been presented, such as GeoDNN [33], VelocityGAN[35], and InversionNet[36].

In our previous study, we proposed SeisInvNet [37] to accurately invert the subsurface velocity distribution from observation data collected from the ground surface. To tackle the challenges in mapping the time-series seismic wave signals to spatial images, SeisInvNet utilizes convolutional layers to encode the observation setup, neighborhood information, and global context of a single-shot seismic profile into one single seismic trace, which forms an embedding vector. Each embedding vector, which contains a variety of seismic information, is then fused via fully connected layers to form a spatially aligned feature map of different seismic traces. Then, the velocity model is reconstructed from all feature maps by a CNN called the Velocity Model Decoder. These DNN-based methods provide new perspectives for the GPR inversion problem.

B. DNNs for GPR image to sub-surface image transformation

So far, studies employing DNNs to map a GPR B-Scan image to a subsurface image have been rare. To the best of our knowledge, the only published study so far was by Alvarez et al. [42]. In their paper, three different state-of-the-art deep learning architectures were employed to reconstruct subsurface images of concrete sewer pipes from B-Scan images. The architectures of the three DNNs, including encoder-decoder (Enc-Dec), U-Net, and Generation Aggressive Network (GAN), are identical to the architectures implemented in [43]. They also evaluated and compared the use of different loss metrics. The validations were conducted on synthetic data. The synthetic GPR B-Scan data and sub-surface permittivity map were reformatted into image pairs. Specifically, each GPR B-Scan

was reformatted to an image with size 125×125 pixels, which corresponds to a concrete segment with the dimensions of 250×250 mm.

Comparative studies have demonstrated that Enc-Dec networks using a differential structural similarity (DSSIM) loss function slightly outperform U-Net and GAN for this GPR image to image transformation. The Enc-Dec network implemented in their paper consisted of an encoder and a corresponding decoder. Each convolutional layer employs a 4×4 convolutional filter with a stride of 2 for downsampling the input image. Subsurface images containing defects with regular geometries (triangles, circles, and rectangles) have been reconstructed effectively. This work demonstrates the feasibility of utilizing DNNs to map a GPR image to a subsurface image. Although the permittivity maps of the subsurface structure have not been reconstructed in their study, it still provides a base for further exploring the application of deep learning for GPR inversion.

III. METHODOLOGY

A. Characteristics of DNN-based GPR inversion task

The DNN-based inversion method is a data-driven non-linear mapping problem [35]. The aim is to find the transformation

$$H: P \rightarrow D \qquad (1)$$

that reconstructs a permittivity map of the tunnel lining structure P^i from the corresponding GPR B-Scan D^i, where $i \in [1,N]$ (N is the number of B-Scan images). Each permittivity model P^i has size $[H; W]$, where H represents depth and W represents the width of the permittivity model. Each GPR B-Scan D^i has dimension $[T; R]$, where T and R denote the time step and the number of traces, respectively. The B-Scan D^i consists of R single GPR traces (A-Scans). We denote the rth single trace on the B-Scan D^i as $D^i r$, where $r \in [1,R]$. Generally speaking, the single GPR trace $D^i r$ provides elapsed information along the depth of the tunnel lining. The data recorded at each time step in the single trace $D^i r$ are related to the dielectric properties at different depths. The different single traces $D^i r, r \in [1,R]$ correspond to the dielectric properties $P^i r*, r* \in [1,W]$ at different detection distances along the width direction of the permittivity map. The schematic is shown in Fig. 1.

The challenges of DNN-based GPR inversion are two-fold. First, because the tunnel lining may contain rebar, the dielectric distribution is usually inhomogeneous. Consequently, the GPR B-Scan data of the tunnel lining are very complex. In particular, the rebar inside the tunnel lining may mask the effective GPR echoes from defects, which manifests in the B-Scan as clutter, as can be seen in Fig. 2. Moreover, tunnel lining defects always have irregular geometries, and defects with different shapes may contribute to similar B-Scan profiles under the impact of multiple waves and scattering. In such cases, it is challenging to accurately reconstruct the details of the tunnel lining defects with different shapes, especially those under rebar. Thus, a network with strong feature extracting capacity is required to make full use of the input data and to learn effective features from the complex B-Scan images. Secondly, there is no specific

spatial alignment between the input (GPR B-Scan) and output (relative permittivity model) images. This is particularly significant in DNN-based inversion, as most existing DNN methods are designed for spatially aligned data pairs. Generally speaking, the position at which a hyperbolic echo exists on a GPR profile may not correspond to any abnormalities in the dielectric model. As can be seen in Fig. 2, the echo induced by the multiple reflection of rebar does not align to any abnormality on the dielectric model. On the contrary, the signals induced by a defect in the dielectric model are always observed not only in its corresponding trace, but also in several adjacent GPR traces. That is to say, the dielectric model at one location is not only related to the corresponding GPR trace, but also to several adjacent GPR traces.
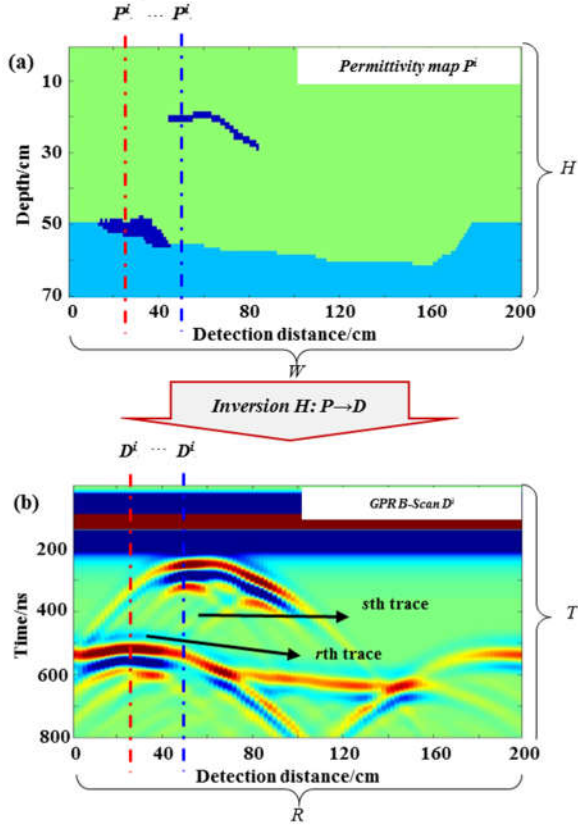

Fig. 1. Schematic of GPR inversion. The permittivity map is shown in (a), and the corresponding GPR B-Scan is shown in (b). D^i_r and D^i_r are the rth trace and the sth trace on the GPR B-Scan respectively; P^i_{r*} is the $r*$th column of permittivity values spatially aligned to D^i_r, and P^i_{s*} is the $s*$th column of permittivity values spatially aligned to D^i_r.

Some end-to-end DNN frameworks designed for image synthesis, such as Enc-Dec, U-Net, and GAN, can be employed to map GPR B-Scan data to a permittivity image. However, the existing networks were all originally designed for images pairs that are spatially aligned, such as photos and medical images. These networks employ fixed convolutional kernels and encode the input data into a feature vector, from which the decoder reconstructs the output [37]. With the increase of the dimension in the feature maps, the spatial features may be gradually lost, which may mean the details or boundaries cannot be reconstructed accurately [44]. For GPR data without a specific spatial alignment, existing DNNs may not be the optimal choice, and a deep learning network that explicitly considers the

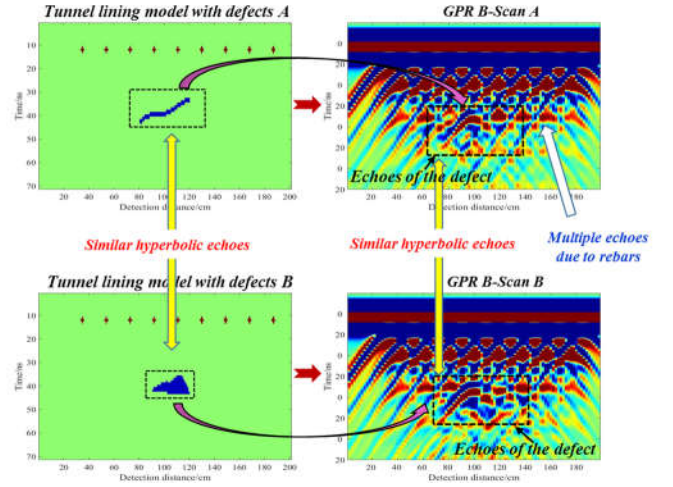characteristics of GPR data may be preferable.

Fig. 2. Two B-Scan and tunnel lining model pairs. Tunnel lining models A and B contains two different defects under rebar, the B-Scan images are complex, and the B-Scan images of the two models are quite similar.

B. Architecture of GPRInvNet

In this paper, we propose a novel DNN architecture for GPR inversion called GPRInvNet, which is able to make full use of the information in the B-Scan and retain the spatial alignment between input and output. The idea of GPRInvNet is inspired by SeisInvNet, which was proposed by us [37], but we improved the network to take specific account of the characteristics of GPR data. Considering the complexity of a GPR B-Scan of tunnel lining, we increased the feature extraction component of the network to extract features from the complex B-Scan data as well as enhancing the information of each trace using the information of its adjacent traces. Additionally, given the special spatial alignment characteristics between the GPR data and the permittivity map, we separately condense the features of each trace, which is spatially aligned to a column of the permittivity map. Then, each column of the permittivity map is reconstructed accurately from the features of each trace. The whole permittivity map can be obtained by splicing all the slices of the permittivity map.

Fig. 3 shows the architecture of GPRInvNet. GPRInvNet consists of a specially designed encoder and a corresponding decoder. The decoder is topologically identical to the decoder component in SeisInvNet [37]. The key component of GPRInvNet lies in its encoder, which is described as a "trace-to-trace" encoder. In the encoding process, we first employ multiple convolutional layers to enrich the information of each GPR trace without compressing its spatial dimension. We have increased the number of convolutional layers as per the GPR data to enhance the capacity of feature extraction. This allows the network to make full use of the information from adjacent traces and automatically learn features from complex B-Scan data. Moreover, because the GPR signals based on electromagnetic waves show a faster decay in amplitude compared with the seismic waves, the useful signals that can be observed in adjacent traces may not be detected in remote traces. Therefore, we only fuse the effective information from the neighboring traces rather than extracting global context from
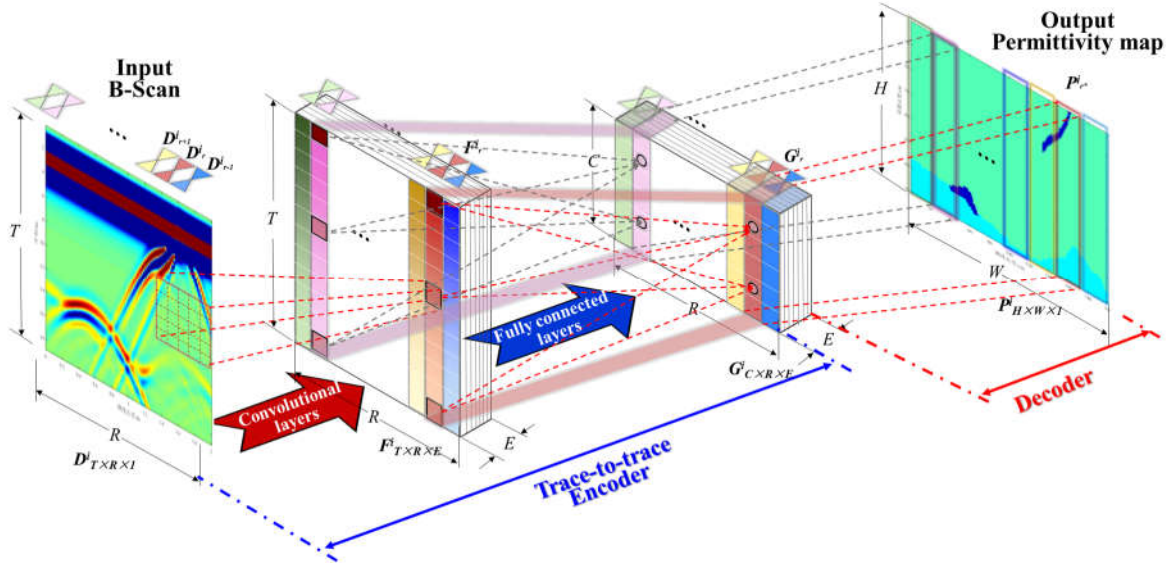
Fig. 3. Architecture of GPRInvNet. D^i with dimension of T×R×1 is the input B-Scan data, F^i with dimension of T×R×E is the feature maps after convolutional layers, a group of features F_r^i spatially aligned to D_r^i contains information extracted from the adjacent traces of D_r^i. G^i with dimension of C×R×E is formed by separately condensoing each column of F^i using fully connected layers, and G_r^i corresponding to the compressed features of F_r^i. P_r^i is a part of permittivity map spatially aligned to G_r^i, and the output of the network P^i with dimension of H×W×1 is the reconstructed permittivity map from D^i.

the entire B-Scan, which prevents our network from learning ineffective features.

After features have been enhanced, several fully connected layers are utilized in the encoding process to condense the features of each trace separately. We artificially align the enhanced features of each trace to a column of the permittivity map. In this paper, we use the term "sensitive zone" to refer to the column of the permittivity map spatially aligning to the enhanced features of each trace. This operation allows our network to accurately reconstruct the details of its sensitive zone.

In the decoding process, we reconstruct the high-quality sensitive zone of each trace and splice all the inverted sensitive zones together to form a permittivity map. GPRInvNet can make the best use of the GPR data, accurately reconstruct the shapes and details of the defects, and generate high-quality dielectric images directly from raw GPR data. Moreover, as we encode the feature trace by trace, the permittivity map can be reconstructed column by column. GPRInvNet is not constrained by the number of traces, and it is capable of inverting B-Scan with an arbitrary number of GPR traces.

The architecture of GPRInvNet as well as its implementation will be described in this section. As the trace-to-trace encoder is specially designed for GPR data inversion, we will introduce the encoding process in detail. However, the decoder is conventional, and it is topologically identical to the decoder component in SeisInvNet. Therefore, we will only briefly present the decoder and the loss function of the network.

C. Trace-to-trace Encoder:

In this paper, we describe the encoder of GPRInvNet as a trace-to-trace encoder. This is because it enriches the information of each trace and condenses the features of each trace separately. The encoder consists of 5 convolutional layers and 5 fully connected layers.

The convolutional layers are employed to generate a feature map F, which not only has the same dimension as the input B-Scan, but also contains knowledge extracted from several adjacent GPR traces. This is inspired by the fact that the echoes of one abnormality are often mainly observed in several adjacent traces of the GPR B-Scan. To be specific, 5×5 convolutional kernels with stride 1 are employed in each layer to extract adjacent information from a GPR B-Scan $D^i_{T×R×1}$. We also tried 3×3 and 7×7 convolutional kernels, but the results are underperformed those employing 5×5 convolutional kernels. After 5 convolutional layers, a feature map $F^i_{T×R×E}$ with the same spatial dimensions as the input GPR B-Scans $D^i_{T×R×1}$ is generated. Here, $F^i_{T×R×E}$ signifies the feature maps encoded from the ith GPR B-Scan, and E denotes the number of feature channels. The feature map F has the same dimension as the input, but the feature at each position contains its neighborhood information. For the GPR data of each trace D^i_r with dimension $[T; 1]$, the convolutional layers convert it into a feature vector F^i_r with dimensions $[T; E]$. Each F^i_r is spatially aligned to a column of the permittivity map to be inverted. The feature map $F^i_{T×R×E}$ can be treated as R columns of feature vectors of the rth GPR trace F^i_r.

Unlike SeisInvNet which encodes the embedded features into a feature map, GPRInvNet encodes the features of each trace separately and splice the features of all the traces to form a group of feature maps. This is implemented by using the fully connected layers to separately condense the feature vector of each trace F^i_r. The design of the fully connected layers in GPRInvNet arose from the need to maintain the spatial alignment between the input B-Scan and output permittivity map. For each encoded GPR trace F^i_r with dimensions $[T; E]$, we adopt five fully connected layers to fuse the time dimensional features of each trace and combine them into features maps with dimensions $[C; E]$. Each fully connected layer includes activation and batch normalization operations. The fully connected layers are implemented for all R feature vectors of the feature map $F^i_{T×R×E}$. In this way, new feature

maps $G^i{}_{C\times R\times E}$, which have the same dimension ratio as the permittivity map P^i, are generated. The rth column vector of this new feature map is denoted as $G^i{}_r$, where $G^i{}_r$ is of size $C\times E$. We artificially enforce each $G^i{}_r$ to be spatially aligned to a column of the permittivity map to be inverted.

Our trace-to-trace encoder has two benefits for GPR inversion in comparison to existing networks: (1) it makes the best use of the raw GPR data by using the convolutional layers to enhance the effective information of each trace from its adjacent traces, and (2) it retains the spatial alignment between the B-Scan and permittivity map by encoding the features of each trace separately.

D. Decoder and loss function:

In the encoder, feature maps $G^i{}_{C\times R\times E}$ with the same dimension ratio as the permittivity map to be inverted $P^i{}_{H\times W}$ are generated. More importantly, the features of each GPR trace $G^i{}_r$ are spatial aligned to sensitive zones in the permittivity map $P^i{}_{r*}$, where $r*\in[1,W]$. With these features, it is easy to accurately reconstruct high-quality dielectric images.

The decoder employed in this study is similar to that of SeisInvNet [37]. We adjust the parameters of the decoder network on the basis of the permittivity map to be reconstructed. It consists of a 4×4 up-convolution, six 3×3 convolutions, and one up-sampling operation. A 4×4 up-convolution with stride 2 is first deployed to enlarge the dimension of the feature maps. This is followed by a 3×3 convolution with stride 1 to stabilize the information. Then, we utilize an up-sampling operation to form feature maps with the same dimension as the permittivity map. Finally, four 3×3 convolutional kernels with stride 1 are added to condense the dimension of the feature channels. Dropout has been employed to randomly abandon some feature maps to avoid over-fitting and improve the robustness of the network. In principle, each feature map $G^i{}_r$ with size $C\times E$ is utilized to accurately invert a small piece of permittivity model $P^i{}_{r*}$, which has size $H\times1$. The whole permittivity map P^i is reconstructed accurately by splicing all $P^i{}_{r*}$ together.

Regarding the loss function, we employ a combination of the L2 norm and multi-scale structural similarity (MSSIM) to minimize the misfit between the input and output images. The loss function is calculated following [37],[45]:

$$L_i(D^i,P^i)=\sum_{h=1}^{H}\sum_{w=1}^{W}\|D^i_{(h,w)}-P^i_{(h,w)}\|_2-\sum_{r\in R}\sum_{h=1}^{H}\sum_{w=1}^{W}\lambda_r SSIM(D^i_{x_{((h,w),r)}},P^i_{y_{((h,w),r)}}) \quad (2)$$

where D and P are the inversion result and ground truth for ith data pair, respectively, $x_{((h,w),r)}$ and $y_{((h,w),r)}$ are the two corresponding windows centered on (h,w) with size r, where $h\in[1,H]$, $w\in[1,W]$. R is the total number of scales. λ_r is the weight of scale r. By minimizing the norm metric and maximizing $MSSIM$ simultaneously, we optimize the model in both structural similarity and per pixel error in the output image.

IV. NUMERICAL SIMULATION

A. Building the Dataset

To provide sufficient data for training GPRInvNet, numerical simulations were conducted to generate synthetic data for the common types of tunnel lining defects, including lining voids,

cracks, lining-rock delamination, leakages, and non-compactness of concrete. The dataset basically covers the common types of tunnel lining defects with irregular shapes. More specifically, it consists of four categories with different configurations of defects: (1) tunnel lining (concrete and rock) containing only rebar or one defect (lining voids, cracks, lining-rock delamination, or non-compactness); (2) tunnel lining with both rebar layer and one defect; (3) tunnel lining containing multiple defects; and (4) tunnel lining with rebar layer and multiple defects. For each category, we considered both air and water as media of the defects, and permitivities for the ground and concrete were chosen from a range. In total, a dataset with 432,000 pairs of data was built. Each data pair included a GPR B-Scan as the input and a permittivity model as the ground truth. There were five different media involved: air, surrounding rock, concrete, water, and rebar. The parameters utilized in the simulation are listed in Table I, which are selected and modified from [46].

TABLE I
RELATIVE DIELECTRIC CONSTANT AND CONDUCTIVITY PROPERTIES

Media	Relative dielectric constant	Conductivity S/m
Air	1	0
Water	81	0.0005
Concrete	8~10	0.0001
Surrounding rock	6~8	0.001
Rebar	300	10^8

The GPR modeling was performed based on finite difference time domain (FDTD) methods using in-house MATLAB code. In the numerical simulation, a permittivity model with width 2.0 m and depth 0.7m was built. A convolutional perfectly matched layer (CPML) was employed to mitigate the impact of boundary effects. The spatial size of the FDTD forward grid was 0.01 m, and the CPMLs occupied 10 meshes. Thus, each permittivity map consisted of 90×220 meshes, which includes 70×200 meshes of the tunnel lining and outer 10 meshes of the CPMLs surrounding the tunnel lining. The source wavelet was the Ricker wavelet with center frequency 600 MHz, and a total of 99 traces of data were obtained from each model. The total time step was 800 with a time window of 2.3587e^{-11}s.

One of the main contributions of this study is the reconstruction of the permittivity map of various tunnel lining defects with irregular geometries. Hence, the shapes of the simulated lining defects are relatively irregular to show the applicability of our proposed GPRInvNet for inverting various shapes of defects. During the simulation, we first modeled the background that included concrete, surrounding rock, and rebar. The interfaces of the surrounding rock were generated by fitting randomly deployed nodes at the bottom of the model using the secondary spline curves. The rebar layer was located in the range of 5 to 25 cm with intervals randomly selected from 15 cm to 30 cm. To simulate practical conditions in the tunnel lining as closely as possible, the dielectric parameters of the concrete and rock were randomly selected from the ranges listed in Table I.

After the background was modeled, we generated the common types of tunnel lining defects with irregular shapes by fitting the constraint nodes using spline curves. The sizes of the

voids were from 16×5 cm to 60×40 cm, and the lengths of the cracks were from 20 to 60 cm. To simulate the lining-rock delamination defect, we first randomly located its position along the interface between concrete and rock. Then, the same method for modeling the void defect was employed to form delamination defects with sizes ranging from 16×5 cm to 100×40 cm. For the non-compactness defects, a section with size ranging from 20×20 cm to 60×60 cm was randomly selected; then, many small voids were generated within the selected section. All defects were randomly distributed in the permittivity map.

B. Experimental Process

We randomly assigned each configuration of defects to the training data, validation data, and testing data with ratio 10:1:1. Thus, a dataset with a total of 432,000 data pairs was randomly divided into three sub-datasets, including 360,000 for training, 36,000 for validation, and 36,000 for testing. Each B-Scan D_i was of size of 800×90, and the corresponding permittivity model P_i had dimensions 90×220. The outer 10 layers of P_i are CPMLs which were cropped from the permittivity model. Finally, we obtained an output permittivity model with dimensions 70×200, which corresponds to a tunnel lining of 0.7×2 m.

TABLE II
DETAILS OF THE GPRINVNET

Stage	Layer	Type	Filter	Strid	Output Size
Encoder	L1	conv	5×5	1	800×99×4
	L2	conv	5×5	1	800×99×8
	L3	conv	5×5	1	800×99×16
	L4	conv	5×5	1	800×99×32
	L5	conv	5×5	1	800×99×64
	L6	FC	1024	1	1024×99×64
	L7	FC	512	1	512×99×64
	L8	FC	256	1	256×99×64
	L9	FC	256	1	256×99×64
	L10	FC	45	1	45×99×64
Decoder	L11	Up-conv	4×4	2	90×198×128
		conv	3×3	1	90×198×128
	L12	Upsample	-	-	90×220×128
		conv	3×3	1	90×220×64
	L13	conv	3×3	1	90×220×64
		conv	3×3	1	90×220×32
	L14	conv	3×3	1	90×220×32
		conv	3×3	1	90×220×1

The details of each layer of GPRInvNet in this study are listed in Table II. The experiments were conducted on an Intel Xeon (R) Gold 5118 CPU workstation with 64 GB RAM and a GTX 1080 Ti GPU. GPRInvNet was implemented based on Pytorch [47]. To optimize GPRInvNet, an Adam optimizer with batch size 12 was applied with learning rate of 5e^{-5}. The dropout rate in the decoder was 0.2. GPRInvNet had 2,041,326 parameters and could be trained end-to-end. The models were trained for 100 epochs, which was observed to be more than sufficient to ensure convergence. Following convention, we saved the parameters that performed best on the validation set and conducted experiments on the validation and test sets.

To quantitatively evaluate the performance of GPRInvNet, a series of metrics were employed. We quantified the misfit error of the inversion results based on mean average error (MAE) and mean square error (MSE) [37]. We also measured the similarity of the local structures by MSSIM [45] and SSIM[48].

C. Comparative study and results

To verify the superiority of the proposed method in reconstructing the permittivity map of a tunnel lining containing complex internal defects, a comparative study was performed based on synthetic GPR data. We chose both physics-driven and data-driven methods as our baselines. GPRInvNet was compared against the DNN-based model Enc-Dec as well as the widely used physics-driven method FWI. All methods were tested on the same testing dataset, and some comparative results are shown in Fig. 4 and Fig. 5. The inversion results for relatively simple tunnel lining defects are displayed in Fig. 4. Figs. 4 (a-1), (b-1), (c-1), and (d-1) and Figs. 5 (a-1), (b-1), (c-1), and (d-1) are the ground truths. The permittivity maps reconstructed using FWI are shown in Figs. 4 (a-2), (b-2), (c-2), and (d-2) and Figs. 5 (a-2), (b-2), (c-2), and (d-2). The inversion results of the Enc-Dec are shown in Figs. 4 (a-3), (b-3), (c-3), (d-3) and Figs. 5 (a-3), (b-3), (c-3), and (d-3). Figs. 4 (a-4), (b-4), (c-4), (d-4) and Figs. 5 (a-4), (b-4), (c-4), and (d-4) provide the results reconstructed using GPRInvNet.

D. Comparison with Enc-Dec Network

The Enc-Dec network, which was initially developed for image segmentation, was employed for mapping the GPR B-Scan image to the subsurface image of concrete in [42]. The image-to-image translation is similar to the inversion task, except that the inversion provides not only a subsurface image but also permittivity values. The Enc-Dec network outperforms U-Net and GAN for imaging the subsurface defects according to aforementioned paper. Therefore, the Enc-Dec network was chosen as a baseline model.

Enc-Dec in this study had the same architecture as in [35],[36]. It consists of an encoder and a corresponding decoder. Each convolutional layer employs a 4×4 convolutional filter with a stride of 2 for downsampling the input image, batch normalization, and element-wise rectified-linear non-linearity (ReLU) to extract features from GPR B-Scan images. Accordingly, the decoder recovers the defects from the embedding vector. 4×4 transposed convolutions with stride 2 were employed to upsample the vector. The loss function was DSSIM[42], and we set the initial learning rate as 5e^{-5}.

Both Enc-Dec and GPRInvNet were trained on the same dataset for 100 epochs. To maintain sufficient physical information in the input and output data, we directly employed the raw data pairs to train the network rather than reformatting them into images. Thus, the input and output of the Enc-Dec network in this study were both data containing concrete physics meaning rather than pixels in the images. The input B-Scan data was resized into a matrix with dimensions [256,128], and the output permittivity maps were resized from [128,256] to [90,220].
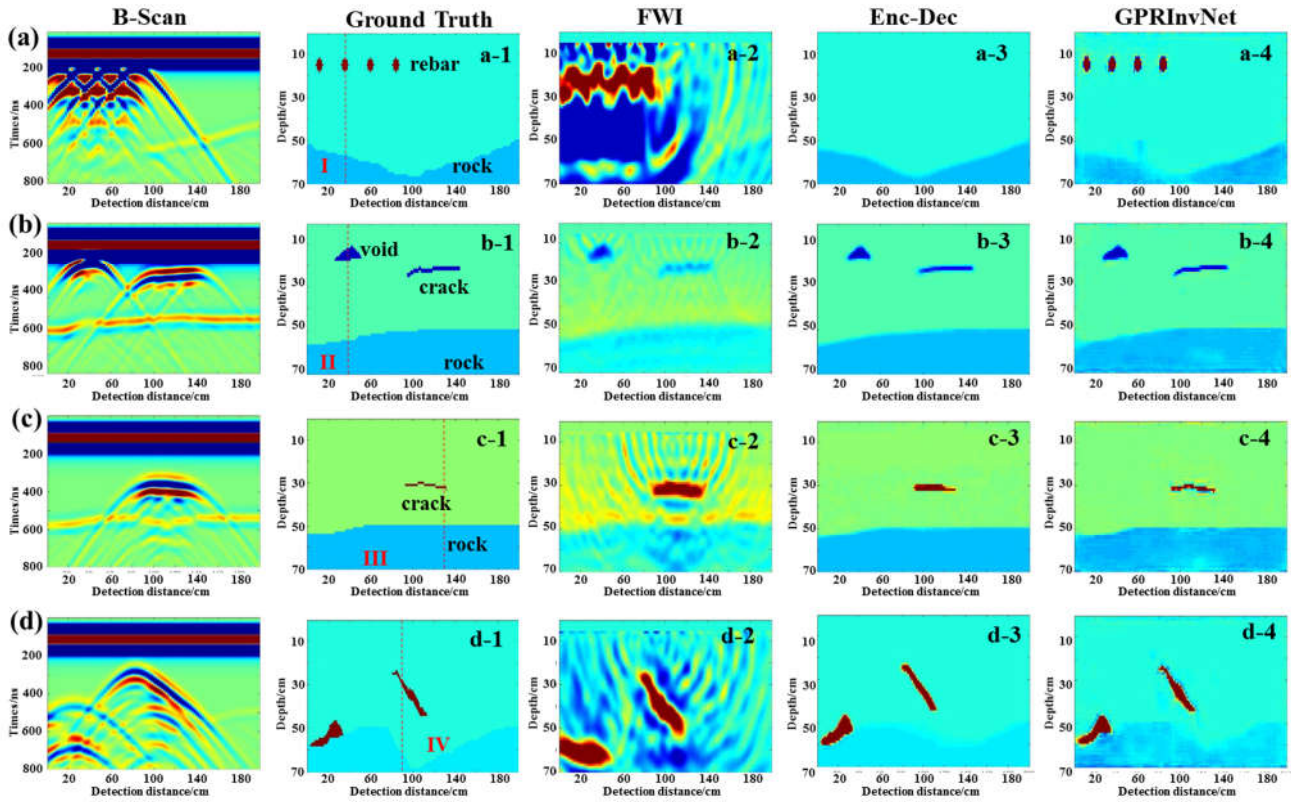
Fig. 4. Inversion results for simple tunnel lining defects. (a) depicts a tunnel lining with rebar only; (b) depicts a tunnel lining with anhydrous defects; (c) depicts a tunnel lining containing one water-bearing defect; (d) depicts a tunnel lining with multiple water-bearing defects. The images of the first column are B-Scan; the images of the second column are groundtruths; the inversion results of FWI, Enc-Dec and GPRInvNet are illustrated in the images of the third, fourth and fifth columns respectively. Lines I to IV are four cutting lines.

Fig. 5. Inversion results for complex tunnel lining defects. (a) depicts a tunnel lining with non-compactness and delamination; (b) depicts a tunnel lining with anhydrous defects under rebar; (c) depicts a tunnel lining containing one water-bearing crack under rebar; (d) depicts a tunnel lining with non-compactness under rebar. The images of the first column are B-Scan; the images of the second column are groundtruths; the inversion results of FWI, Enc-Dec and GPRInvNet are illustrated in the images of the third, fourth and fifth columns respectively. Lines I to IV are four cutting lines.
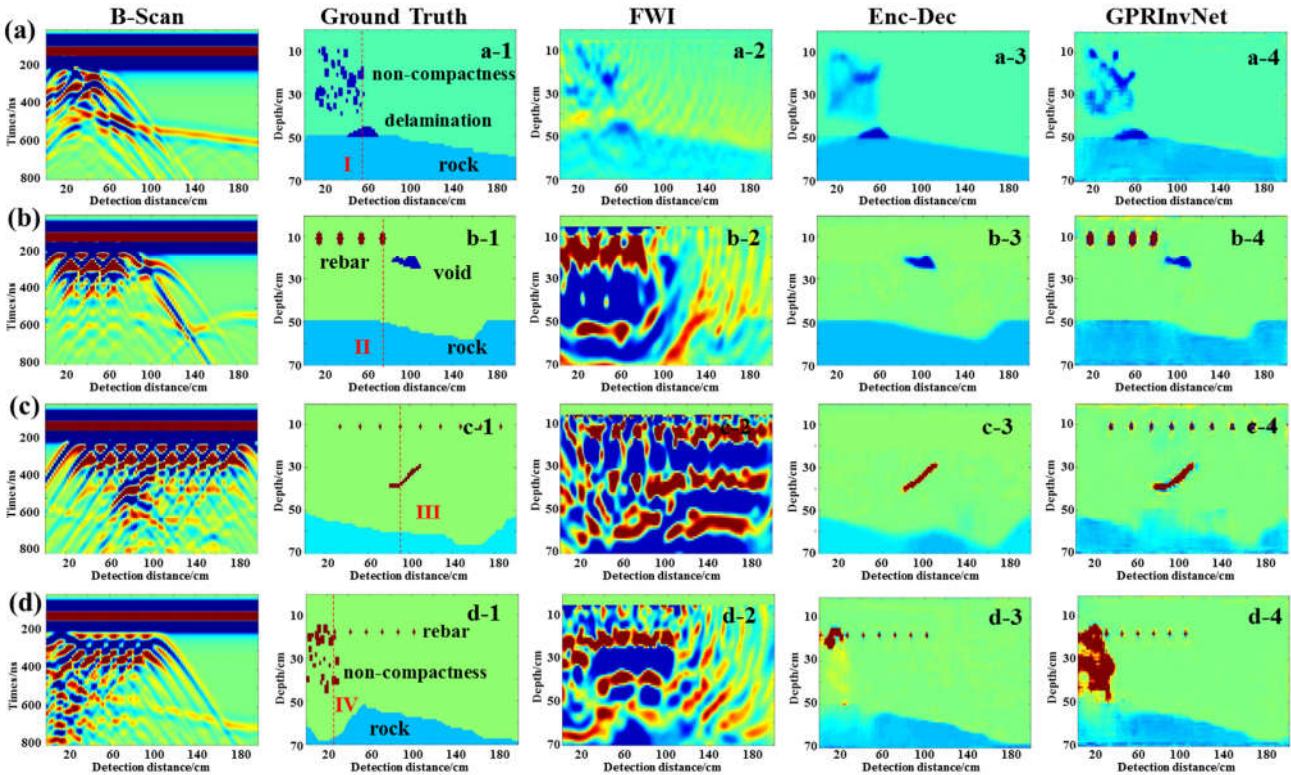
As can be seen from Fig. 4, Enc-Dec was capable of reconstructing the interfaces between rock and concrete as well as some simple defects, such as cracks, voids, and delamination without rebar. However, the reconstructed defects typically had blurred boundaries. More importantly, it could not reconstruct rebar, as shown in Fig. 4 (a-3). In contrast, GPRInvNet successfully reconstructed the rebar and tunnel lining defects with relatively clear boundaries. The shapes of anhydrous cracks, anhydrous voids, water-bearing cracks, rebar, and surrounding rocks reconstructed by GPRInvNet were highly consistent with the ground truths.

For tunnel linings with complex defects, such as non-compactness, defects under the rebar, etc., GPRInvNet clearly outperformed Enc-Dec. As can be seen in Figs. 5 (b) and (c), Enc-Dec failed to recover the rebar. This is probably because the size of each rebar is very small, so Enc-Dec failed to learn the features of rebar during the feature extraction process. For the non-compactness (Fig. 5 (a)) and water-bearing non-compactness defects under rebar (Fig. 5 (d)), because the honeycomb obstructed the propagation of electromagnetic waves, neither method could perfectly recover the shapes of defects. As shown in Figs. 5 (a) and (d), Enc-Dec could only partially recover the defect with a very blurry region. In contrast, GPRInvNet successfully provided complete profiles of the complex non-compactness defects (Fig. 5 (a-4)) even if the defects were below the rebar (Fig. 5 (d-4)). Although the shapes of the complex defects reconstructed by GPRInvNet were not completely consistent with the ground truths, it still provided the best inversion results.

To quantitatively evaluate the performances of the two DNN-based methods, the evaluation metrics on the validation set and test set are listed in Table III. In general, GPRInvNet achieved the best performance. On the test set, the MAE, MES, SSIM,

and MSSIM of GPRInvNet were 0.00286, 0.000374, 0.973784, and 0.980623, respectively. They are obviously better than Enc-Dec's, which were 0.004895, 0.002515, 0.949639, and 0.858237. In general, GPRInvN showed consistent superiority according to all evaluation metrics compared.

Therefore, GPRInvNet outperformed Enc-Dec in GPR inversion. The shapes and details of the defects reconstructed by GPRInvNet are obviously better than those reconstructed by Enc-Dec. This is due to the specially designed encoding approach of GPRInvNet, which can make full use of the information during extraction of the feature map as well as retaining the spatial alignment between the input and output. On the contrary, Enc-Dec employs a fixed convolutional kernel to extract the feature map as well as compressing the dimension. This may lose detailed information, such as the features of small-sized rebars and the boundaries of defects. Moreover, Enc-Dec decodes the permittivity map from the vector, which may contribute to the loss of spatial information.

TABLE III
COMPARISON OF EVALUATION METRICS

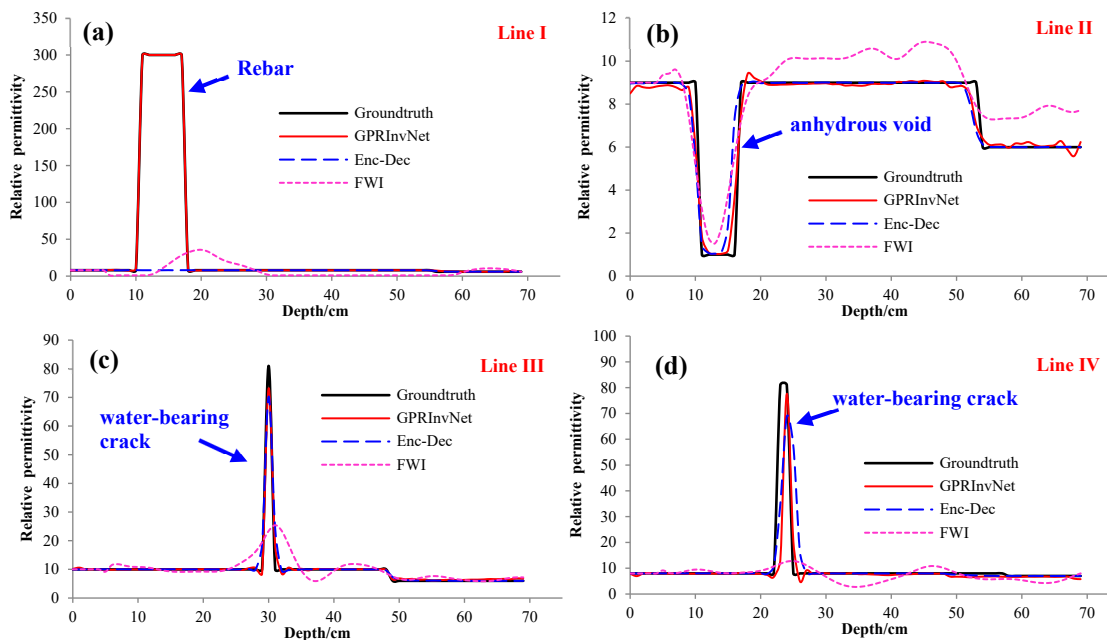| Dataset	Metrics	GPRInvNet	Enc_Dec
Valid	MAE ↓	**0.002845**	0.004927
	MSE ↓	**0.000368**	0.002539
	SSIM ↑	**0.973808**	0.949326
	MSSIM ↑	**0.980597**	0.855101
Test	MAE ↓	**0.002860**	0.004895
	MSE ↓	**0.000374**	0.002515
	SSIM ↑	**0.973784**	0.949639
	MSSIM ↑	**0.980623**	0.858237

Fig. 6. Comparison of inverted permittivity values along the depth of the tunnel linings for simple tunnel lining defects . (a), (b), (c) and (d) depicts the inverted relative permittivity values of cutting lines I to IV on Fig. 4 respectively.

E. Comparison with conversational FWI

FWI reconstructs dielectric properties using all received waveforms by minimizing the difference between the forward modeling waveform and observed waveform [13]. To demonstrate the superiority of GPRInvNet, a comparative study against the widely-used FWI was performed and is reported in this section. As we can see from Fig. 4, FWI can roughly determine the approximate distribution of cracks, voids, and delamination in non-reinforced concrete with blurred boundaries. The inversion results of the anhydrous defects (Fig. 4 (a-2)) are slightly better than those of the water-bearing defects (Figs. 4 (c-2) and (d-2)). However, FWI completely missed the surrounding rock and defects under rebar, as shown in Fig. 4 (b-2). In contrast, GPRInvNet could still reconstruct the defects under rebar.

For the complex defects, FWI provided the best inversion results in reconstructing the anhydrous non-compactness. However, it still underperformed GPRInvNet. Comparing Fig. 5 (a-2) with Fig. 5 (a-4), FWI tends to present blurred profiles of non-compactness defects, while GPRInvNet provides relatively accurate detailed structures. For defects under rebar, it is apparent that FWI fails to reconstruct both anhydrous defects and water-bearing defects deployed in reinforced concrete, as is shown in Figs. 5 (b-2), (c-2), and (d-2). This is probably due to the mask of rebar on the defects; most electromagnetic waves are reflected by rebar. In such situations, FWI could rarely achieve optimal parameters. However, GPRInvNet provided more satisfying results and clear boundaries of defects, even if the defects were under the rebar. Thus, the overall performance of GPRInvNet is better than that of the traditional FWI.

In terms of the computational cost, FWI took approximately 20 min to complete inversion for a single B-Scan image. In contrast, a well-trained GPRInvNet is capable of inverting one image within approximately 0.027 sec. Although training the neural network is a computationally intensive process, it takes place only once. The well-trained GPRInvNet can be used with near-real-time speed for GPR inversion.

F. Comparison of permittivity values

To further analyze the inversion effects, we compared the permittivity values of the aforementioned methods. The relative permittivity values were extracted along the cutting lines. The cutting lines were numbered from I to IV, as shown in Fig. 4 and Fig. 5. The relative permittivity values along the cutting lines of Fig. 4 and Fig. 5 are shown in Fig. 6 and Fig. 7 respectively.

As shown in Fig. 6 and Fig. 7, the inversion curves of permittivity through GPRInvNet are essentially the same as those of the ground truth, except that the amplitude is slightly different. Compared with Enc-Dec and FWI, we can find that for all the common defects, the oscillation of permittivity reconstructed by GPRInvNet is effectively alleviated and closer to the real values. Taking the line IV in Fig. 7 as an example, GPRInvNet successfully predicted the variation of permittivity at a depth of 40 cm, while the remaining methods mis-detected it. FWI gave the worst results, as shown in Fig. 6 and Fig. 7 (pink line). It can be observed that the relative permittivity values of defects under rebar and water-bearing defects predicted by FWI are always away from the true values. Compared with the DNN-based method, the permittivity curves reconstructed using traditional FWI show great fluctuations. The performance of Enc-Dec was better than that of FWI, but it still underperformed GPRInvNet. For some water-bearing defects, the results of Enc-Deck differed greatly from the real results in terms of the general trend of permittivity change (Fig. 7; Line IV). Moreover, Enc-Dec failed to reconstruct the permittivity of rebar. Therefore, the overall performance of GPRInvNet was better than that of Enc-Dec as well as the widely used FWI method.
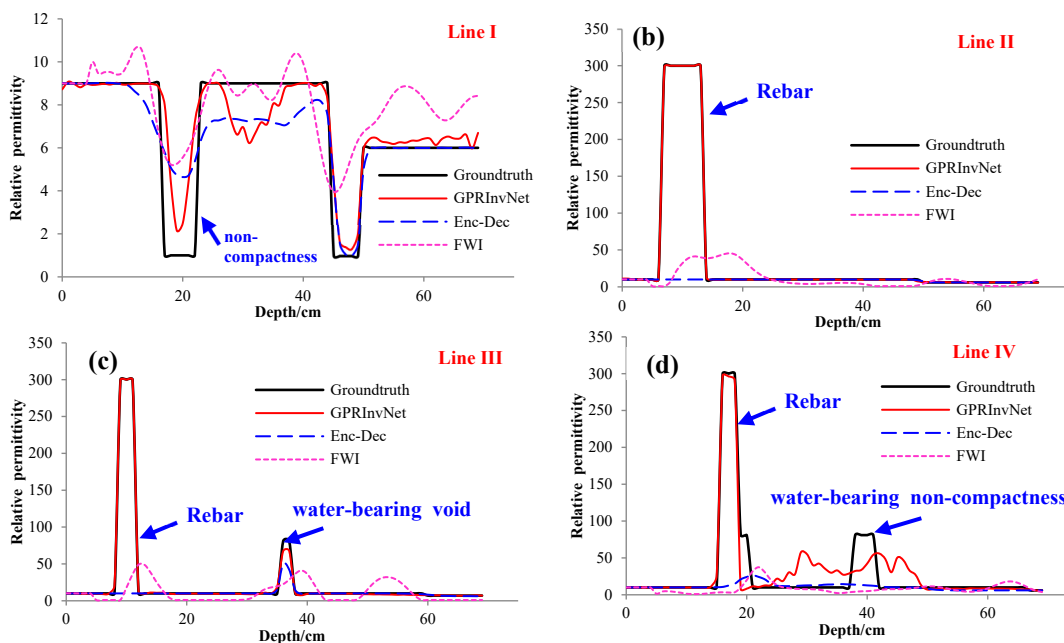

Fig. 7. Comparison of inverted permittivity values along the depth of the tunnel linings for complex tunnel lining defects. (a), (b), (c) and (d) depicts the inverted relative permitivity values of cutting lines I to IV on Fig. 4 respectively.

We also looked closer at the permittivity measured for different filling materials and compared the inversion results at pixel level. The inverted results with maximum error for anhydrous defects lie in Fig. 7 Line I at a depth of 20 cm. The relative permittivity of the anhydrous defects inverted by GPRInvNet was approximately 2, which is close to the true value of 1, while at the same location, the inverted permittivity values by Enc-Dec and FWI were 4 and 5, respectively.

For GPRInvNet, the inverted value of rebar with the maximum deviation can be found in Line IV of Fig. 7. The inverted value is 296, which is quite close to the true value of 300 in the simulation. In contrast, the result of rebar provided by FWI with the best performance was 70, and Enc-Dec totally failed in recognizing rebar. For the water-bearing defects, the results reconstructed using GPRInvNet were also close to the true values. For example, the true relative permittivity at a depth of 10 cm in Fig.7 Line IV is 80. The permittivity provided by GPRInvNet was approximately 78, while the result of Enc-Dec was 68. Even for the water-bearing defects below the rebar (Line IV at a depth of 40 cm), only GPRInvNet predicted the variation of the permittivity. Although the predicted value of 40 was smaller than the true value, it still performed better than other methods. In general, we can come to the conclusion that GPRInvNet outperform other methods in quantitatively inverting permittivity values.

V. EXPERIMENTS ON REAL DATA

The previous section demonstrated the superiority of GPRInvNet on synthetic data. The question remains of can it be used for real data? Real GPR data is much more complex, and currently there is no available real data for training a data-driven DNN model. In this section, a method is presented to generalize the trained GPRInvNet using synthetic data on real data. A model experiment was performed to validate the feasibility.

A. Model testing

To validate the performance of GPRInvNet on real data, model testing was conducted. A concrete experimental model with approximate dimensions of 4×2×0.7m (length×width×height) was built, as shown in Fig. 8. In the middle part of the concrete model did not contain any defects, which is called as a non-defect zone in this study. The remaining part of the model was divided into several zones with approximate dimensions of 0.7×0.7×0.7m for different experiments. For our experiment, we deployed rebar, cracks,

and voids in different zones of the concrete. A hollow acrylic box with dimensions 400×600×20 mm was deployed in the concrete as the anhydrous crack (Fig. 8 (a)). A waterproof plastic box with dimensions 400×600×200 mm was utilized as a void (Fig. 8 (b)). We filled it up with water to simulate water-bearing defects. The crack defect was deployed on the superficial layer at a depth of approximately 20 cm. The water-bearing defect was placed on the bottom of the model. There were four rebars with a diameter of 16 mm in the concrete model, which were located at intervals of approximately 15 cm. We also made the distance between two defects large enough to avoid interference of two signals as well as to mitigate the impact of movement during the pouring of concrete. Three of them were at a depth of approximately 15 cm, and the remaining one was located at a depth of 20 cm. The experiments were carried out 41 days after the concrete model was formed.

Fig. 8. Schematic diagram of testing model and defects. (a) depicts the waterproof box for simulating void; (b) depicts the acrylic box for simulating crack; (c) shows the GPR system utilized in the experiment; (d) is the model testing and the deployment of defects.

To penetrate the concrete with depth of 0.7m, we utilized MALA Impluse Radar with the central frequency of 600 MHz in our experiment, as shown in Fig. 8. The instrument integrates an antenna with its logger and transmits the recorded data via WiFi to a tablet PC. The data can be displayed in real-time in the format of B-Scan images. The logged data can also be imported to a computer and be further analyzed with professional software. We set the sampling point to 512 under the "Wheel" mode. The trace interval was 0.02 m.

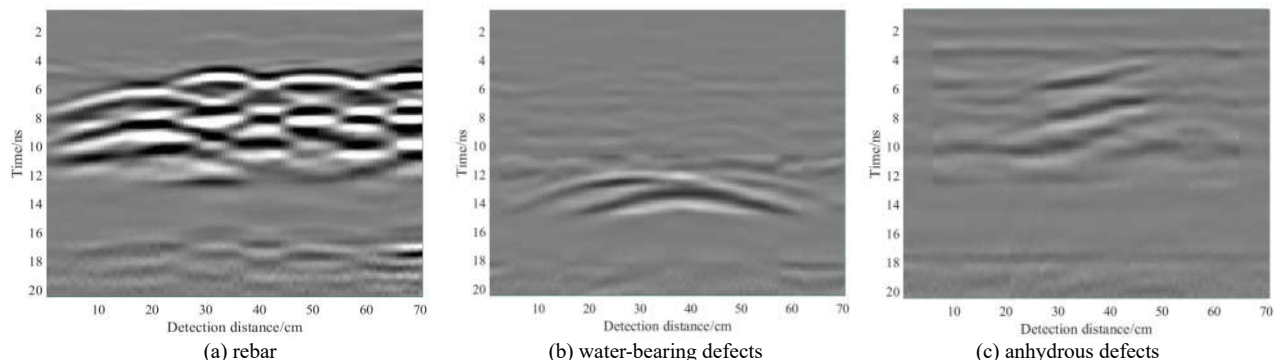|		
(a) rebar	(b) water-bearing defects	(c) anhydrous defects

Fig. 9. GPR B-Scan images from the experiments. (a) is the B-Scan image of rebar; (b) is the B-Scan image of water-bearing defects; (c) is the B-Scan image of anhydrous defect

B. Data processing

Due to the inhomogeneity of the practical structure to be detected and the impact of noises in the real environment, the detected real GPR B-Scan was more complicated than the synthetic data. We logged GPR B-Scan data from the non-defect zone of the concrete experimental model as background noise. Then we added the background noise of real data recorded form the concrete model into the synthetic B-Scan data to train GPRInvNet. Therefore, in our experiment, not only the B-Scan data with defects but also those without any defects in the concrete were recorded. The B-Scan data containing defects were only for testing, and the B-Scan containing background noise were employed in the training process of GPRInvNet.

Before we integrated real data into the synthetic B-Scan data, data preprocessing was performed on real data. The preprocessing included several operations, such as static correction, direct component removal, gain adjusting, background removal, filtering, and averaging. The B-Scan images for the rebar and defects after preprocessing are shown in Fig. 9.
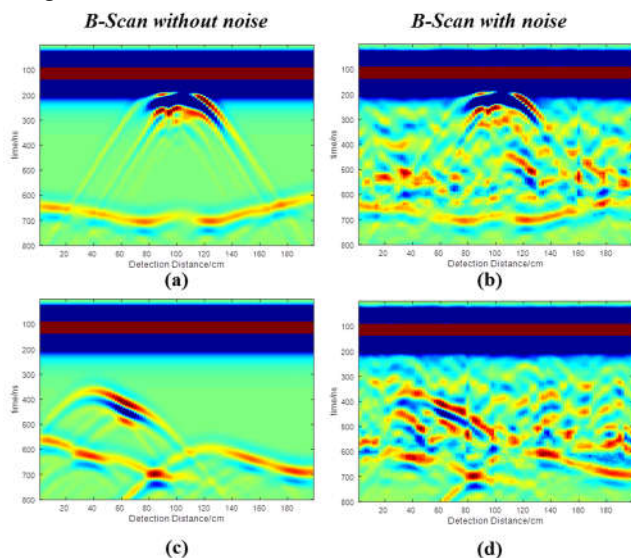

Fig. 10.   B-Scan data with background noise patches. (a) and (c) are two synthetic B-Scan data; (b) is the synthetic B-Scan data of (a) with real background noises; (d) is the synthetic B-Scan data of (c) with real background noises.

The real B-Scan data containing only background noise were preprocessed. After that, we employed interpolation to enlarge the dimension of the real data and a sliding window to randomly crop the background noise patches. A total of 187 background noise patches with dimensions 800×99 were obtained at this step. Then we performed amplitude normalization for both background noise patches and synthetic data. During the normalization, the maximum amplitudes of the B-Scan were multiplied by a weight coefficient, which was randomly selected in the range of 0.5 to 2, so as to increase the diversity of the data. Finally, the data of normalized background noise patches and synthetic B-Scan images were added per pixel to form a new B-Scan with noises. Fig. 10 depicts some of the data with and without background noise.

GPRInvNet was retrained on the new dataset for 100 epochs. By adding the real background patches with synthetic data in the training and validation data sets, we hoped that GPRInvNet would learn information, such as the inhomogeneity of the practical medium and the interference of noise in the real environment. Note that there was no real data in the new training dataset, and GPRInvNet was never trained using real data depicting hyperbolic echoes induced by defects.

C. Experimental results and analysis

We tested the retrained GPRInvNet on real B-Scan data of the defects. The performances of GPRInvNet, Enc-Dec, and FWI were compared. The comparative results of different methods are shown in Fig. 11. The inversion results for anhydrous cracks are presented in Fig. 11 (a). While Fig. 11 (b) and (c) depict the inversion results for rebar and water-bearing void, respectively.

As can be seen in Fig. 11, the overall performance of GPRInvNet was better than that of Enc-Dec and FWI, even for the real data. The shapes of rebar, anhydrous crack, and water-bearing void inverted using GPRInvNet were almost identical to the ground truths. GPRInvNet successfully reconstructed the locations and profiles of the four rebars (Fig. 11 (a-4)). On the contrary, Enc-Dec completely missed the rebar layer (Fig. 11 (a-3)), and FWI could only determine the approximate distribution range of rebar rather than their shapes (Fig. 11 (a-2)). Meanwhile, the water-bearing defect was well reconstructed by GPRInvNet, as shown in Fig. 11 (b-4). Enc-Dec only reconstructed part of the defect, while FWI completely missed the water-bearing defect on the bottom of the model. For the anhydrous crack, all three methods were capable of inverting the profile of the defect, as can be seen in Fig. 11 (c), though the shape of the crack reconstructed by GPRInvNet was closer to the true model. For the rebar and water-bearing defects, GPRInvNet obviously outperformed the other two methods. Although the boundaries of the inverted defects were slightly blurred due to inhomogeneity of the concrete in the experiment, GPRInvNet could still provide rough profiles for these common types of defects.

Overall, GPRInvNet provided the best performance, especially for rebar and water-bearing defects. Moreover, the experimental results indicate that GPRInvNet trained only on synthetic data could be generalized on real GPR data by adding real background patches into the training dataset.
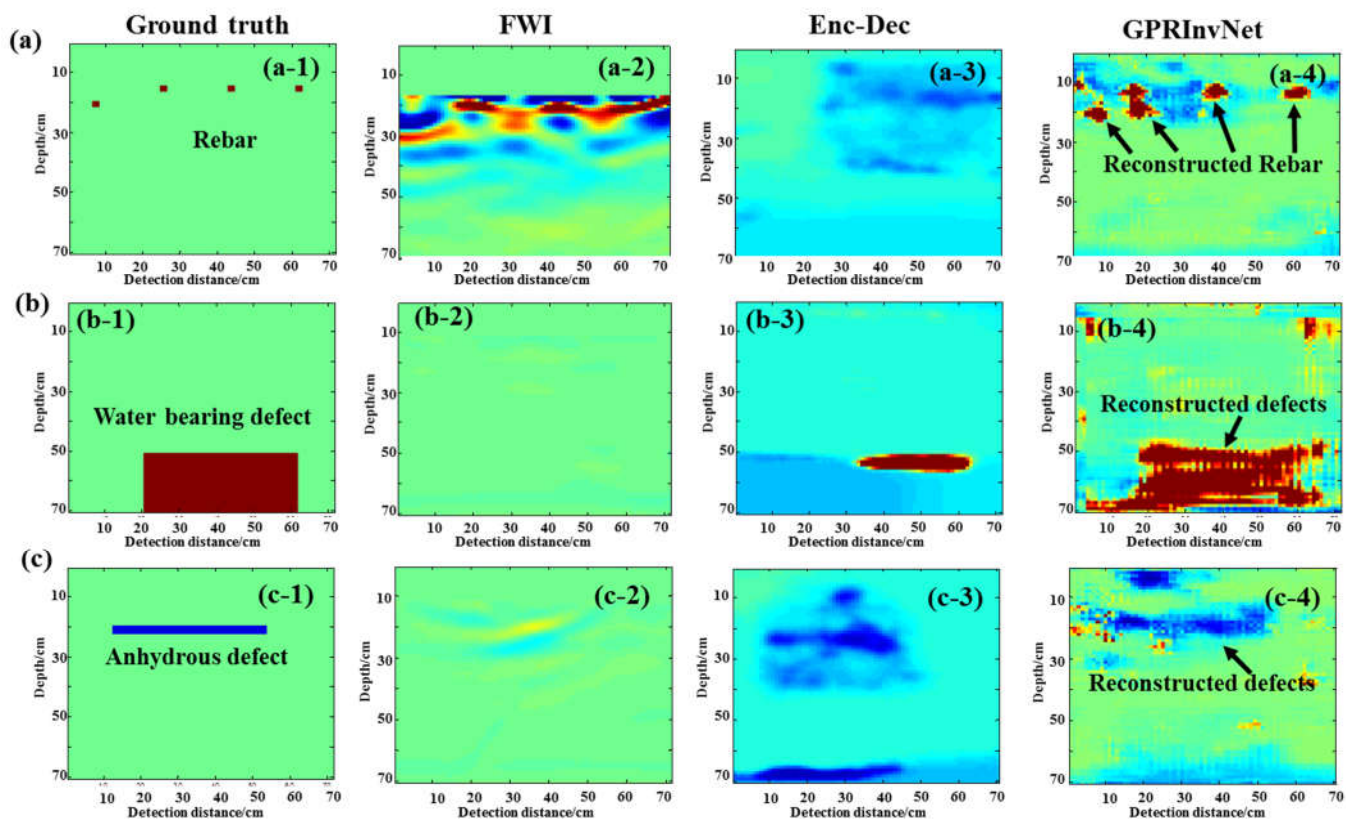
Fig. 11. Inversion results of the experimental data. (a) depicts the groundtruth and inversion results of concrete with rebar only; (b) depicts the groundtruth and inversion results of concrete with water-bearing defect; (c) shows the groundtruth and inversion results of concrete with anhydrous defects.

VI. CONCLUSION

In this paper, a novel DNN-based architecture called GPRInvNet was proposed for reconstructing high-quality relative permittivity maps of tunnel lining from GPR data. GPRInvNet includes a specially designed encoder for GPR data to make full use of the GPR recording as well as to retain the spatial alignment between the B-Scan and permittivity map. It has clear potential significance in improving the reconstruction of tunnel lining defects and assessing the status of complex lining defects. Furthermore, the network has the potential to be employed for inverting GPR data in other GPR related applications, provided sufficient training data is available.

GPRInvNet was first validated based on synthetic GPR data; we successfully applied GPRInvNet to reconstruct a permittivity map of tunnel linings containing complex defects with irregular geometries. It is capable of effectively reconstructing the dielectric properties and shapes of common types of tunnel lining defects with clear boundaries. Comparative results demonstrate that GPRInvNet outperforms existing baseline methods.

The performance of GPRInvNet was also verified by experiments on real GPR data. A method was introduced to transfer GPRInvNet, which is trained starting from purely synthetic data, to real GPR data. Experimental results validated that GPRInvNet effectively inverted the tunnel lining defects, particularly rebar and water-bearing defects, based on real data. It was also shown that GPRInvNet generalized well to real GPR

data by adding some background GPR acquisitions to the pool of training data.

However, due to the complexity of real GPR data, only rough profiles of the defects could be reconstructed. And we did not perform validation using field experiments. This issue merits further research.

REFERENCES

[1]. W. W. L. Lai, X. Dérobert, and P. Annan, "A review of ground penetrating radar application in civil engineering: a 30-year journey from locating and testing to imaging and diagnosis," *NDT & E International.*, vol. 96, pp. 58–78, Jun. 2018.
[2]. Z. Huang, and J. Zhang, "Determination of Parameters of Subsurface Layers Using GPR Spectral Inversion Method," *IEEE Transactions on Geoscience and Remote Sensing.*, vol. 52, no. 12, pp. 7527-7533, Dec. 2014.
[3]. Q. Dou, L. Wei, D. R. Magee, and A. G. Cohn, "Real-Time Hyperbola Recognition and Fitting in GPR Data," *IEEE Transactions on Geoscience and Remote Sensing.*, vol. 55, no. 1, pp. 51-62, Jan. 2017.

[4]. A. A. Morteza, and F. Tosti, " GPR applications in structural detailing of a major tunnel using different frequency antenna systems," *Construction and Building*., vol. 158, no. 15, pp. 1111-1122, Jan, 2018.

[5]. F.J. Prego, M. Solla, X. Núñez-Nieto, and P. Arias, " Assessing the applicability of Ground-Penetrating Radar to quality control in tunneling construction," *Journal of Construction Engineering and Management*., vol. 142, no. 5, pp. 06015006, May. 2016.

[6]. N. F. E. Benedetto, M. Bano, A. Tzanis, J. Nyquist, K. Sandmeier, and N. Cassidy, "Advanced ground penetrating radar signal processing techniques," *Signal Process*., vol. 132, pp. 197-200, Mar. 2017.

[7]. L. Travassosa, L. Avilab and N. Ida, "Artificial Neural Networks and Machine Learning techniques applied to Ground Penetrating Radar: A review," *Applied Computing and Informatics*., October 2018. [Online]. Available: https://doi.org/10.1016/j.aci.2018.10.001

[8]. E. Menendez, J. G. Victores, R. Montero, S. Martínez, and C. Balaguer, "Tunnel structural inspection and assessment using an autonomous robotic system," *Automation in Construction*., vol. 87, pp. 117-126, March, 2018.

[9]. G. Parkinson, and C. Ekes, "Ground Penetrating Radar Evaluation of Concrete Tunnel Linings," in *Proceedings of 12th International Conference on Ground Penetrating Radar*, Birmingham, UK, June. 16–19, 2008.

[10]. D. Feng, X. Wang, and B. Zhang, " Specific evaluation of tunnel lining multi-defects by all-refined GPR simulation method using hybrid algorithm of FETD and FDTD," *Construction and Building Materials.*, vol. 185, pp. 220-229, Oct, 2018.

[11]. R. Montero, J. G. Victores, S. Martínez, A. Jardón, and C. Balaguer, " Past, present and future of robotic tunnel inspection, Automation in Construction," *Automation in Construction*., vol. 59, pp. 99-112, Nov, 2015.

[12]. A. Fedeli, M. Pastorino, and A. Randazzo, "Advanced inversion techniques for ground penetrating radar.," *Journal of Telecommunications and Information Technology*., no. 3, pp. 37-42, 2017, [Online]. Available: https://doi.org/10.26636/jtit.2017.119717.

[13]. E. Fisher, G.A. McMechan, and A.P. Annan, "Acquisition and processing of wide aperture ground-penetrating radar data," *Geophysics*., vol. 57, no. 3, pp. 495-504, Mar. 1992.

[14]. G. A. Meles, J. van der Kruk, S. A. Greenhalgh, J. R. Ernst, H. Maurer, and A. G. Green, "A new vector waveform inversion algorithm for simultaneous updating of conductivity and permittivity parameters from combination crosshole/borehole-to-surface GPR data," *IEEE Transactions on Geoscience and Remote Sensing*., vol. 48, no. 9, pp. 3391-3407, Sept. 2010.

[15]. S. Liu, L. Lei, L. Fu, and J. Wu, "Application of pre-stack reverse time migration based on FWI velocity estimation to ground penetrating radar data," *J. Appl. Geophysics*., vol. 107, pp. 1-7, Aug. 2014.

[16]. J. D. Irving, M. D. Knoll, and R. J. Knight, "Improving crosshole radar velocity tomograms: A new approach to incorporating high-angle traveltime data," *Geophysics*., vol. 72, no. 4, pp. J31-J41, Jul. 2007.

[17]. J. van der Kruk, T. Liu, A. Mozaffari, N. Gueting, A. Klotzsche, H. Vereecken, C. Warren, and A. Giannopoulos, " GPR full-waveform inversion, recent developments, and future opportunities," in *2018 17th International Conference on Ground Penetrating Radar (GPR)*, Rapperswil, Switzerland ,June. 18-21.2018.

[18]. S. Busch, J. van der Kruk, and H. Vereecken, "Improved Characterization of Fine-Texture Soils Using On-Ground GPR Full-Waveform Inversion," *IEEE Transactions on Geoscience and Remote Sensing*., vol. 52, no. 7, pp. 3947-3958, Jul. 2014.

[19]. I. Giannakis, A. Giannopoulos, and C. Warren, "Realistic FDTD GPR antenna models optimized using a novel linear/nonlinear full-waveform inversion," *IEEE Transactions on Geoscience and Remote Sensing*., vol. 57, no. 3, pp. 1768-1778, Mar. 2019.

[20]. X. Yang, J. van der Kruk, J. Bikowski, P. Kumbhar, H. Vereecken, and G. A. Meles, "Full-waveform inversion of GPR data in frequency-domain," in *2012 14th International Conference on Ground Penetrating Radar (GPR)*, Shanghai, 2012, pp. 324-328.

[21]. A. Tarantola, "Inversion of seismic-reflection data in the acoustic approximation," *Geophysics*., vol. 49, no. 8, pp. 1259-1266, Aug. 1984.

[22]. Van A., Wielen D., Courard L. and Nguyen F., "Detection of defects in concrete with ground penetrating radar." in *ESPSC 2011 European Symposium on Polymers in Sustainable Construction*, Warsaw., Poland, 2011, pp. 221-225.

[23]. Q. Ren, "Inverts permittivity and conductivity with structural constraint in GPR FWI based on truncated Newton method," *Journal of Applied Geophysics*., vol. 151, pp. 186-193, Apr, 2018.

[24]. D. Feng, X. Wang, and B. Zhang., " Improving reconstruction of tunnel lining defects from ground-penetrating radar profiles by multi-scale inversion and bi-parametric full-waveform inversion," *Advanced Engineering Informatics*., vol. 41, pp. 100931, Aug. 2019.

[25]. F. Zhang, B. Liu, L. Liu, J. Wang, C. Lin, L. Yang, et al., "Application of ground penetrating radar to detect tunnel lining defects based on improved full waveform inversion and reverse time migration. Near Surface Geophysics," *Near Surface Geophysics*., vol. 17, no. 2, pp. 127-139, Feb. 2019.

[26]. Y. LeCun, Y. Bengio, and G. E. Hinton, "Deep learning," *Nature.*, vol.521, no. 7553, pp. 436–444, May, 2015.

[27]. K. Ishitsuka, S. Iso, K. Onishi, and T. Matsuoka. "Object Detection in Ground-Penetrating Radar Images Using a Deep Convolutional Neural Network and Image Set Preparation by Migration," *International Journal of Geophysics.*, Volume 2018, Article ID 9365184 pp. 1-8, Nov,2018.

[28]. S. Ren, K. He, R. Girshick, and J. Sun, "Faster R-CNN: Towards Real-Time Object Detection with Region Proposal Networks," *IEEE Transactions on Pattern Analysis & Machine Intelligence.*, vol. 39, no. 6, pp. 1137-1149, Jun, 2015.

[29]. X. Miao, J. Wang, Z. Wang, Q. Sui, Y. Gao, and P. Jiang, "Automatic Recognition of Highway Tunnel Defects Based on an Improved U-Net Model," *IEEE Sensors Journal.*, vol. 19, pp. 11413-11423, Dec, 2019.

[30]. P. Jiang, F. Gu, Y. Wang, C. Tu, and B. Chen, "Difnet: Semantic segmentation by diffusion networks," in *Advances in Neural Information Processing Systems 31*. Curran Associates, Inc., 2018.

[31]. I. Goodfellow, J. Pouget-Abadie, M. Mirza, B. Xu, D. Warde-Farley, S. Ozair, A. Courville, and Y. Bengio, "Generative adversarial nets" in *Advances in Neural Information Processing Systems*, pp. 2672-2680, 2014.

[32]. V. Das, A. Pollack, U. Wollner, and T. Mukerji, "Convolutional neural network for seismic impedance inversion," in *SEG Technical Program Expanded Abstracts 2018*, Anaheim, CA, USA ,2018, pp. 2071-2075.

[33]. M. Araya-Polo, J. Jennings, A. Adler, and T. Dahlke, "Deep-learning tomography," *The Leading Edge*., vol. 37, no. 1, pp. 58-66, Jan. 2018.

[34]. M. Alfarrajand, G. Alregib, "Semi-supervised Learning for Acoustic Impedance Inversion." *arXiv preprint arXiv*:1905.13412, 2019.

[35]. Z. Zhang, Y. Wu, Z. Zhou, and Y. Lin, "VelocityGAN: Subsurface Velocity Image Estimation Using Conditional Adversarial Networks," in *2019 IEEE Winter Conference on Applications of Computer Vision (WACV)*, Waikoloa Village, HI, USA, 2019. pp. 705-714.

[36]. Y. Wu, Y. Lin, and Z. Zhou, "Inversionnet: Accurate and efficient seismic waveform inversion with convolutional neural networks," in *SEG Technical Program Expanded Abstracts 2018*. Society of Exploration Geophysicists, 2018, pp. 2096–2100.

[37]. S. Li, B. Liu, Y. Ren, Y. Chen, S. Yang, Y. Wang, and P. Jiang, "Deep learning Inversion of Seismic Data, " *arXiv preprint arXiv*: 1901.07733v1.

[38]. M. T. Pham, S. Lefèvre, " Buried object detection from B-scan ground penetrating radar data using Faster-RCNN," in *IGARSS 2018-2018 IEEE International Geoscience and Remote Sensing Symposium*, Valencia, Spain, 2018. pp. 6804-6807.

[39]. K. Dinh, N. Gucunski, and T. H. Duong, "An algorithm for automatic localization and detection of rebars from GPR data of concrete bridge decks," *Automation in Construction*, vol.89, pp. 292–298, May. 2018.

[40]. X. Xu, Y. Lei, Feng, and J. Lanza-Gutiérrez, "Railway Subgrade Defect Automatic Recognition Method Based on Improved Faster RCNN", *Scientific Programming.*, pp. 1-12, June，2018.

[41]. Z. Tong, J. Gao, and H. Zhang, "Recognition location measurement and 3d reconstruction of concealed cracks using convolutional neural networks", *Construction & Building Materials.*, vol. 146, pp. 775-787, Aug, 2017

[42]. J. K. Alvarez and S. Kodagoda, "Application of deep learning image-to-image transformation networks to gpr radargrams for sub-surface imaging in infrastructure monitoring," in *2018 13th IEEE Conference on Industrial Electronics and Applications (ICIEA)*, Wuhan, China, 2018, pp. 611-616.

[43]. P. Isola, J. Y. Zhu, T. Zhou, and A. A. Efros, "Image-to-image translation with conditional adversarial networks," in *2017 IEEE Conference on Computer Vision and Pattern Recognition (CVPR),* Honolulu, HI, USA, 2017, pp. 5967–5976.

[44]. O. Ronneberger, P. Fischer, and T. Brox, "U-Net: Convolutional networks for biomedical image segmentation," in *International Conference on Medical image computing and computer-assisted*

intervention, 2015, pp. 234-241

[45]. Z. Wang, E. P. Simoncelli, and A. C. Bovik, "Multiscale structural similarity for image quality assessment," in *The Thrity-Seventh Asilomar Conference on Signals*, Systems & Computers, vol. 2, pp. 1398-1402, 2003.

[46]. J. L. Davis, and A. P. ANNAN, "45," *Geophysical Prospecting.*, vol. 37, no. 5, pp. 531-551. July. 1989.

[47]. J. K. Huang, T. Jia, D. E. Carlin, and T. Ideker, "pyNBS: a Python implementation for network-based stratification of tumor mutations, Bioinformatics," *Geophysical Prospecting.*, vol. 34, no. 16, pp. 2859–2861.Aug, 2018.

[48]. Z. Wang, A. C. Bovik, H. R. Sheikh, and E. P. Simoncelli, "Image quality assessment: From error measurement to structural similarity," *IEEE Trans. Image Process.*, vol. 13, no. 4, pp. 600-612, 2004.

Bin Liu received his B.S. (2005) and Ph.D. (2010) degree in civil engineering from Shandong University, China. He then joined Geotechnical and Structural Engineering Research Center at Shandong. University, China. Currently, he is a professor in School of Qilu Transportation, Shandong University. He is member of Society of Exploration Geophysicists (SEG) and International Society for Rock Mechanics and Rock Engineering (ISRM), and serves as council member of Chinese Geophysical Society. His research area is engineering geophysical prospecting techniques, especially their applications in tunnels.

Yuxiao Ren received the bachelor's and master's degree in mathematics from Shandong University, China (2014) and Loughborough University, UK(2015), respectively. He then came back to Shandong University and has been studying for his doctoral degree in civil engineering since 2016. Currently, He is a visiting scholar in Georgia Institute of Technology under the supervision of Prof. Felix Herrmann. His research interests include seismic modeling and imaging, full-waveform inversion and deep-learning based geophysical inversion.

Hanchi Liu received the B.E degree in Information and electrical engineering from Shandong University of Architecture and Engineering in 2019. She is now pursuing the Master degree in School of Control Science and Engineering, Shandong University, Shandong, China. Her current research interests include defects recognition and deep learning based geophysical inversion.

Hui Xu received the master's degree in Qilu Transportation from Shandong University, Shandong, China, in 2019. Currently, He is working on 3-D object reconstruction.

Zhengfang Wang received the Ph.D. degree in Measurement technology and automatic instrument from Shandong University, China, in 2014. He is now an Associate Professor with the School of Control Science and Engineering, Shandong University. His current research interests include GPR data processing, detection and diagnosis of infrastructures and optic fiber sensors for infrastructures monitoring.

Anthony G. Cohn is a Full Professor in the School of Computing at the University of Leeds and a Fellow at the Alan Turing Institute in the UK. He is a Fellow of the Royal Academy of Engineering, the Association for Advancement of Artificial Intelligence, and the European Association for Artificial Intelligence. His research interests are in Artificial Intelligence, Knowledge Representation and Reasoning, Cognitive Vision, Robotics, Sensor Fusion, and Decision Support Systems. Since 2014, part of his research has focussed on decision support systems for streetworks and utilities. The VAULT system which provides 24/7 real time integrated utility data across Scotland arising from his Mapping the Underworld and VISTA projects won a IET Innovation Award and a NJUG award for "Avoiding Damage". He has received Distinguished Service awards from IJCAI and AAAI.

Peng Jiang received the B.S. and Ph.D. degrees in computer science and technology from Shandong University, China, in 2010 and 2016, respectively. Currently, He is a research assistant with School of Qilu Transportation, Shandong University, China. His research spans various areas, including computer vision, image processing, machine learning and deep learning. He has published many works on top-tier venues, including ICCV, NeurIPS(NIPS), IEEE TIP, IEEE TGRS, \etc. Recently, he is focusing on deep learning based geophysical inversion.